

Supporting Information for:

3D Imaging of a dislocation loop at the onset of plasticity

in an indented nanocrystal

Maxime Dupraz^{1,*}, *Guillaume Beutier*¹, *Thomas W. Cornelius*², *Guillaume Parry*¹,
*Zhe Ren*², *Stéphane Labat*², *Marie-Ingrid Richard*^{2,3}, *Gilbert A. Chahine*¹, *Oleg*
*Kovalenko*⁴, *Marc De Boissieu*¹, *Eugen Rabkin*⁴, *Marc Verdier*¹, *Olivier Thomas*²

* Current address: Swiss Light Source, Paul Scherrer Institut, CH-5232, Villigen PSI,
Switzerland

E-mail: maxime.dupraz@psi.ch

1. *Univ. Grenoble Alpes, CNRS, Grenoble-INP, SIMAP, F-38000 Grenoble, France*
2. *Aix Marseille Univ., Université de Toulon, CNRS, IM2NP UMR 7334, F-13397 Marseille Cedex 20, France*
3. *ID01/ESRF, 71 Avenue des Martyrs, CS40220, F-38043, Grenoble Cedex 9, France*
4. *Department of Materials Science and Engineering, Technion – Israel Institute of Technology, 32000 Haifa, Israel*

Supporting information S1: Sample preparation and experimental details

The gold particles were obtained employing solid state dewetting of a 30 nm thick Au film on the *c*-plane oriented polished sapphire substrate. The film was deposited using an electron-beam evaporator (Airco Temescal FC 1800) on a lithographically patterned substrate of 2" in diameter (Gavish Inc.). The substrate was ultrasonically cleaned in acetone, ethanol, isopropanol, and DI water prior to the resist coating. The pattern consisted of holes of ~1-2 μm in size in the marked 50 μm pitch grid obtained by standard photolithography procedure including: vapor prime with Hexamethyldisilazane (HMDS), spin coating of resist, soft bake, contact printing exposure using mercury lamp source mask aligner (KARL SUSS MA-6), post bake, development, and hard bake. The lift-off procedure after film deposition was performed at 70 °C in 1-methyl-2-pyrrolidone (NMP) for 3 min, followed by rinsing in acetone, ethanol, isopropanol and DI water. The samples were annealed in the tube resistance furnace in ambient air for 24 h at 900 °C, resulting in agglomeration of the patterned film and formation of single crystalline faceted Au particles of different sizes (100-500 nm in height and 200-2000 nm in lateral size). Some fraction of the isolated center gold islands evolved into single isolated particles which were imaged and mapped by scanning electron microscopy (HR-SEM, Zeiss Ultra Plus) for the later BCDI experiment (Fig. S1a-b). The lithographic/mask processing route ensured that only one crystallite is irradiated by the incoming X-ray beam. This was important since any partial illumination of neighboring crystallite would cause interferences in the measured CXD patterns.

The obtained crystallites exhibited the same well-defined out-of-plane orientation as the original thin Au film, with the Au [1 1 1] direction being normal to the (0 0 0 1) sapphire surface. The crystallites also exhibited a low degree of in-plane ordering, the preferred orientation corresponding to the lowest energy of Au-sapphire interface¹. Precise localization of the sample was achieved by Scanning X-ray Diffraction Microscopy (SXDM) in a continuous scanning mode, allowing the fast acquisition of two-dimensional real space maps at the vicinity of the sample of interest².

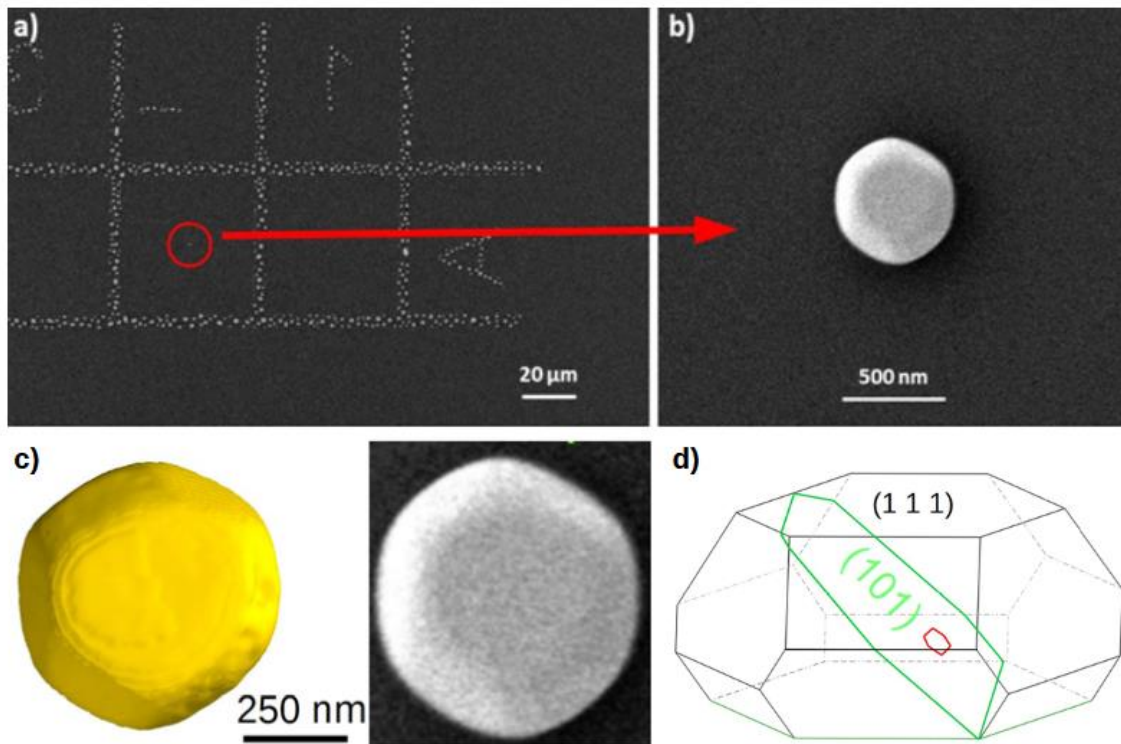


Figure S1 SEM images of the solid state dewetted gold particles. The mask used for the deposition of the gold thin film allows obtaining a regular array of crystals with a single and isolated particle at the centre of each square. (b) Zoom of the gold particle that was selected for the in-situ nanoindentation experiment. (c) Comparison between a low resolution SEM image of the sample and the reconstructed electron density drawn at 25% of the maximum of density. (d) Schematics of the crystal. The (101) crystallographic plane containing the dislocation loop is indicated in green. The loop itself is highlighted in red.

Supporting information S2: Details on the AFM tip

The AFM cantilever is actually a so-called Akiyama-probe (Fig. S2) that was provided by NanoAndMore company. Its specifications are listed in Table S2. The radius of curvature of the AFM-tip of less than 15 nm ensures that the surface area over which the force is applied remains relatively small. Applied forces by the AFM are estimated from the cantilever elastic stiffness (5 N/m) times the chosen imposed vertical displacement (10-100nm) considering that the indentation depth is much smaller than the displacement.

Tab. S1 Cantilever and tip specifications

Cantilever	Length: 310 μm , Thickness: 3.7 μm , Width: 30 μm each Material: n ⁺ silicon (0.01-0.25 Ohm.cm)
Tip	Tip radius < 15 nm, height: 28 μm
Force constant	5 N/m (Si cantilever)
Resonant frequency	50 kHz

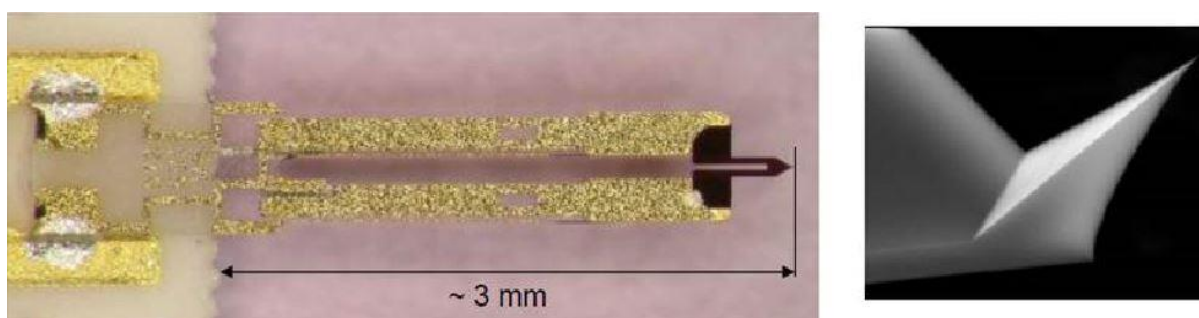


Figure S2 Left: Picture of the cantilever, right: SEM image of the tip (from Akiyama)

Supporting information S3: Bragg Coherent Diffraction Imaging: experimental set-up and methods

The experiment was performed at beamline ID01 of the ESRF, with a monochromatic beam of 8 keV. Transverse coherence was enforced by high-precision slits matching the transverse coherence lengths (70 μm H x 300 μm V) just before the focusing optics. The coherent beam was focused down to 700 x 400 nm^2 (HxV), using a tungsten Fresnel zone plate (FZP) with a diameter of 300 μm and an outer zone width of 70 nm. To ensure a full illumination of the crystal of interest, it was placed 1 mm behind the focus. The diffracted X-rays were recorded using a two-dimensional detector (Maxipix, 516 x 516 pixels of 55 μm) mounted 1.02 m downstream from the sample position. The 3D diffraction patterns around the Au 1 1 1 Bragg reflection are built by stacking 250 slices of the 2D detector collected by rocking the sample across the Bragg reflection over a $\pm 0.5^\circ$ range with a step size of 0.004° (for a total acquisition time of the order of 20 min). The resolution in reciprocal space is $2.2 \mu\text{m}^{-1} \times 2.2 \mu\text{m}^{-1} \times 1.9 \mu\text{m}^{-1}$, hence an oversampling of the order of 3 in each dimension for an object of the order of 1 μm .

Due to the Bragg geometry ($\theta_{\text{Bragg}}=19.2^\circ$ at 8 keV), the natural frame of the 3D data sets is not orthogonal (the scan direction is not orthogonal to the detector plane). It was thus interpolated onto an orthogonal frame with approximately the same voxel size, where the subsequent analysis is performed. The 3D dataset was then cropped in each of the two pixel detector directions and subsequently binned by a factor of 2 along all three dimensions, resulting in a 200x200x200 pixels dataset which was used for the reconstruction.

To avoid any linear phase ramp in the complex sample density, $\rho(\mathbf{r})$ induced by a mis-centering of the reciprocal space data, its Fourier transform $F(\mathbf{q})$ was re-centred to the nearest pixel using the centre of mass of $|A(\mathbf{q})|^4$ ³. Sub pixel shifting was achieved by multiplying $\rho(\mathbf{r})$ by the appropriate phase ramp calculated from the centre of mass. The maximum phase shift accounting from refraction effects was calculated⁴ to a value of 0.45 radians, much smaller than the phase variations at the vicinity of the defects, and was thus neglected. The particle was illuminated with a beam size of 700x400 nm^2 (HxV), slightly larger than the size of the particle (550x550x275 nm^3). For a sample positioned exactly in the focal spot of the Fresnel zone plate, the phase of the wave front is expected to be flat in the focus⁵⁻⁷, however under such experimental conditions, Diaz *et al.* reported distortions of the wave front of as much as 0.5 radians⁸. Here, the sample was placed out of the focus of the Fresnel Zone plate by 1 mm, where the distortions of the wave front were expected to be even larger. Linear phase variations observed at the vicinity of the {1 1 1} and {0 0 1} facets (Fig. S4) can be ascribed to the variations in the phase of the illumination wavefront. In order to disentangle the contribution of the strain and of the illumination wavefront in the overall phase variations, the latter would need to be reconstructed by performing a 2D ptychographic scan of the particle⁹. Such reconstruction has not been performed during the experiment; therefore the phase variations observed in the sample originate from both contributions.

To quantify the phase variations induced by the illumination wavefront, we performed a simulation of the illumination wavefront with the experimental parameters listed in Tab. S3. In good agreement with our experimental observations, the phase is mostly flat vertically over 400 nm, which is slightly more than the height of the crystal (Fig. S3a). On the other hand, it appears that the phase is not constant over the full width

of the crystal, explaining the phase ramp observed on one side of the crystal (Fig. S4). As a comparison, we also included the reconstruction of the wavefront performed during a subsequent experiment with a similar experimental setup (Fig. S3b). The reconstruction was performed in transmission geometry on a well-known reference object using the PyNX code ¹⁰. The phase profile is in reasonably good agreement with our simulations. In conclusion, the phase variations induced by the wave front are significantly smaller than the phase variations caused by strain and crystal defects, and the presence of these phase inhomogeneities do not affect the result and conclusions presented in this work.

Tab. S2 Experimental parameters used for the simulation of the wavefront

Beamstop diameter	50 μm
OSA diameter	50 μm
FZP diameter / thickness / width of the outer ring	300 μm / 1.8 μm / 70 nm
Opening of the coherence slits	70(H) x 300(V)
Distance coherence slits-FZP	10.4 cm
Distance FZP - OSA	11.1 cm

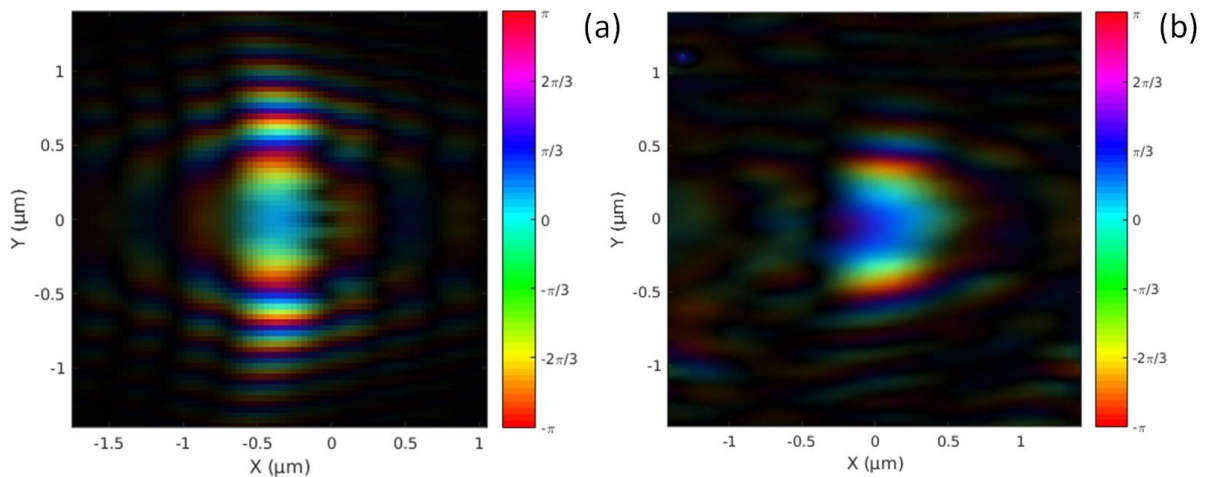


Figure S3 a) Simulated wavefront 1mm behind the focal plane using the experimental parameters listed in Tab. S3 b) Reconstructed wavefront during a subsequent experiment using a similar experimental set-up (courtesy of Steven Leake, ID01 beamline, ESRF)

The reconstruction of the CDI data was carried-out using standard phase retrieval algorithms namely the error-reduction (ER) ¹¹, hybrid input-output (HIO) ¹² and shrink-wrap (SW) algorithms ¹³. In the phase retrieval procedure, both reciprocal space and real space are updated at each step of the algorithm and constraints are applied on both sides. Inputs of the algorithms are the measured intensity and a finite size 3D support in which all the complex sample density is constrained. Here

this support was given by the Patterson function (autocorrelation of the diffracted intensity), threshold to 2% of its maximal value¹³. The latter gives a good estimation of the size of the object for weakly strained objects. The procedure for the phase retrieval consisted of an alternation of 50 ER and 100 HIO repeated 100 times. The HIO feedback parameter β was set to a typical value of 0.9¹⁴. Shrinkwrapping of the support was done at the end of every series of (50 ER + 100 HIO) *via* convolution of the reconstruction with a Gaussian function with a threshold of 10%. The method was used over 50 random starts for each dataset. The best solutions were selected according to their metric error (which quantifies the agreement between the retrieved and experimental intensities) and to the homogeneity of their electron density¹⁵. To reduce the noise inherent to experimental data, the 10 best reconstructions were averaged to produce the final image of the sample.

The spatial resolution of the experiment was estimated from the phase retrieval transfer function (PRTF)¹⁶:

$$\text{PRTF}(q) = \frac{|\langle F(q) \rangle|}{\sqrt{I(q)}}$$

The resolution is given at the point where the PRTF drops to a particular value. We used a value of $\text{PRTF} = 0.5$, considered as a conservative estimate, to determine the spatial resolution. This gives us a resolution of ~ 13 nm, comparable with values found in the literature^{15,17,18}.

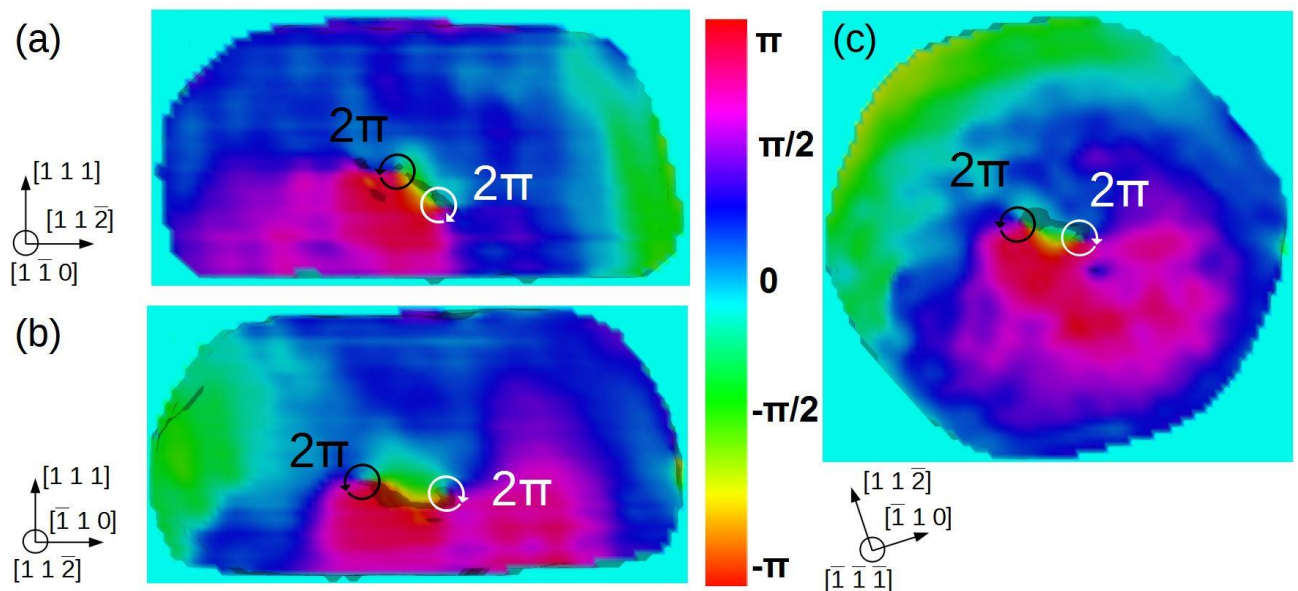


Figure S4 Slices of the reconstructed displacement field in the (1 -1 0) (a), (1 1 -2) (b) and (1 1 1) (c) planes.

The cross-correlation $CC(m, n)$ between two images I_m and I_n presented in Fig. 3 of the manuscript is calculated as $CC(m, n) = \frac{\sum_{pixels} I_m * I_n}{\sqrt{\sum_{pixels} I_m^2 * \sum_{pixels} I_n^2}}$. $CC = 1$ for identical images and lower otherwise.

Supporting information S4: Simulation of nanoindentation on a nickel thin film

To facilitate the identification of the crystal defects nucleated during the indentation experiment, the reconstruction of a dislocation arrangement, resulting from a molecular dynamics simulation of plastic indentation on a nickel thin film was carried out¹⁹. The simulation cell shown in Fig. S5a contains 521642 atoms and measures 173x196x162 Å³. An EAM potential²⁰ was employed to describe the interactions between the nickel atoms. The indenter was modelled by a repulsive sphere with a radius of 120 Å. The indentation was carried out by gradually moving the sphere into the crystal in steps of 0.1 Å along the [-1 -1 -1] direction, while holding fixed the bottom atomic layer of the crystal (non-deformable substrate assumption). Periodic boundary conditions were applied along the [1 0 -1] and [1 -2 1] directions of the cell. Between each increment, the potential energy of the cell was minimized using a Conjugate Gradient algorithm to obtain a succession of quasi-equilibrium states with increasing indentation depths. The indentation resulted in the nucleation of three equivalent variants of interstitial prismatic loops that plastically accommodate the displacement along the [-1 -1 -1] direction of indentation. Their Burgers vectors of the dislocation loops are shown in Fig. S5a

The simulated diffraction data used for the reconstruction was calculated at the vicinity of several 1 1 1 peaks in the kinematic approximation by summing the amplitudes scattered by each atom with its phase factor¹⁰. The 3D dataset in the reciprocal space consists of 128x128x128 pixels, with a step size of 1/128 reciprocal lattice units (0.022 nm⁻¹). The extent of the reciprocal space gives a real space pixel size of 0.28 nm.

The reconstruction procedure is similar to the one described in Supporting Information S1, without the need of averaging the best reconstructions to reduce the noise on the experimental data.

Determination of the slip system of the prismatic loops:

A reliable and efficient way to determine the Burgers vectors of the prismatic dislocation loops relies on the use of the well-known invisibility conditions: $\mathbf{g} \cdot \mathbf{b} = 0$ ²¹⁻²³. This approach was used in our previous work to identify crystal defects from their signature on diffraction patterns²¹. It can also be applied on real space reconstructions. Figure S5.b-d shows an isosurface rendering of the reconstructed electron density (35% threshold of the maximum density) for several 1 1 1 reflections. The dips in the electron density at the vicinity of the loops can be used to confirm the spatial arrangement and Burger vectors of the dislocations. For $\mathbf{g} = 1\ 1\ 1$, none of the invisibility conditions are satisfied, and all the dislocation loops are visible (Figure S5b). On the other hand, for $\mathbf{g} = 1\ -1\ 1$, $\mathbf{g} = 1\ 1\ -1$ and $\mathbf{g} = -1\ 1\ 1$, only one variant is visible since the other two fulfill the invisibility conditions (Figure S5c-d). Independently of the reflection chosen, the position of the dislocation loops in the crystal matches perfectly with the atomistic configuration. Provided that 2 or 3 equivalent 1 1 1 reflections are reconstructed, this approach can thus be used to determine the Burgers vectors of the loops within an isolated crystal in a very reliable way. If a single 1 1 1 Bragg peak is measured, one can deduce the Burgers vector of the loop from its crystallographic orientation, as described in the body of the manuscript.

Finally, the simulation allows to confirm the prismatic nature of the dislocation loops nucleated during the nanoindentation experiment. The profile of the phase shift around the defect is indeed very consistent with the one observed experimentally:

- A pair of vortex-antivortex of phase can be evidenced in the $(1\ 1\ 1)$ plane that intercept the loop in two *loci* (Fig. S5f)
- A π phase jump between the region inside and outside the loop is observed in the $(0\ 1\ 1)$ plane normal to the glide cylinder of the prismatic loop.

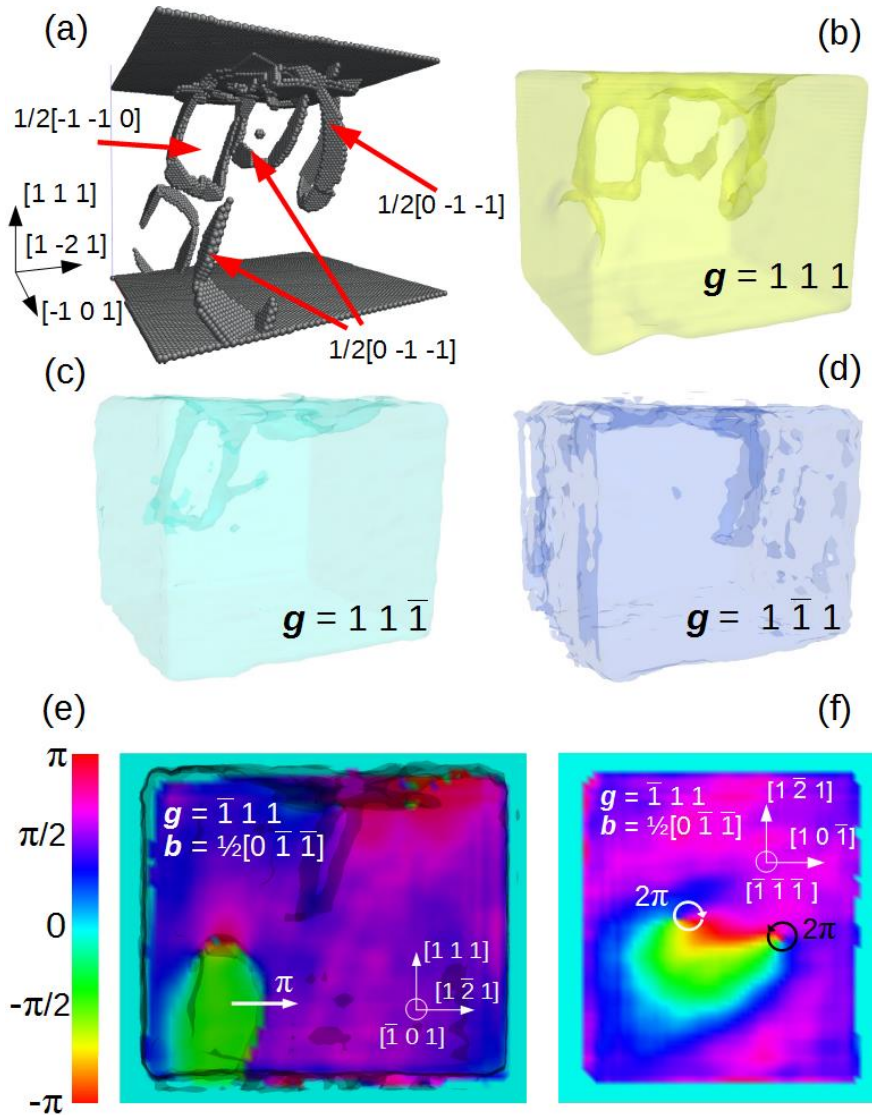


Figure S5 (a) Atomistic configuration of the nickel thin film. (b)-(d) 35% isosurface of the reconstructed electron density which reveals the visibility of the loops for various \mathbf{g} . (e) Simulated $\varphi_{1\bar{1}\bar{1}}$ phase fields in the $(0\ 1\ 1)$ plane normal to the glide cylinder of the prismatic loop. (f) $\varphi_{1\bar{1}\bar{1}}$ phase field in the $(1\ 1\ 1)$ plane intercepting the prismatic loop in two *loci*.

Supporting Information S5: Evolution of ϵ_{zz} for consecutive indentations with increasing load.

We provide here all the measured states of the crystal, after successive indentations of increasing load. The retrieved outer shape of the particle is found to be consistently the same, with sizes matching the AFM and SEM observations, and the internal density does not show any particular feature, except for the void of density observed with the dislocation loop after the 3rd indentation. Here we present the strain component ϵ_{zz} , which is obtained from the retrieved phase.

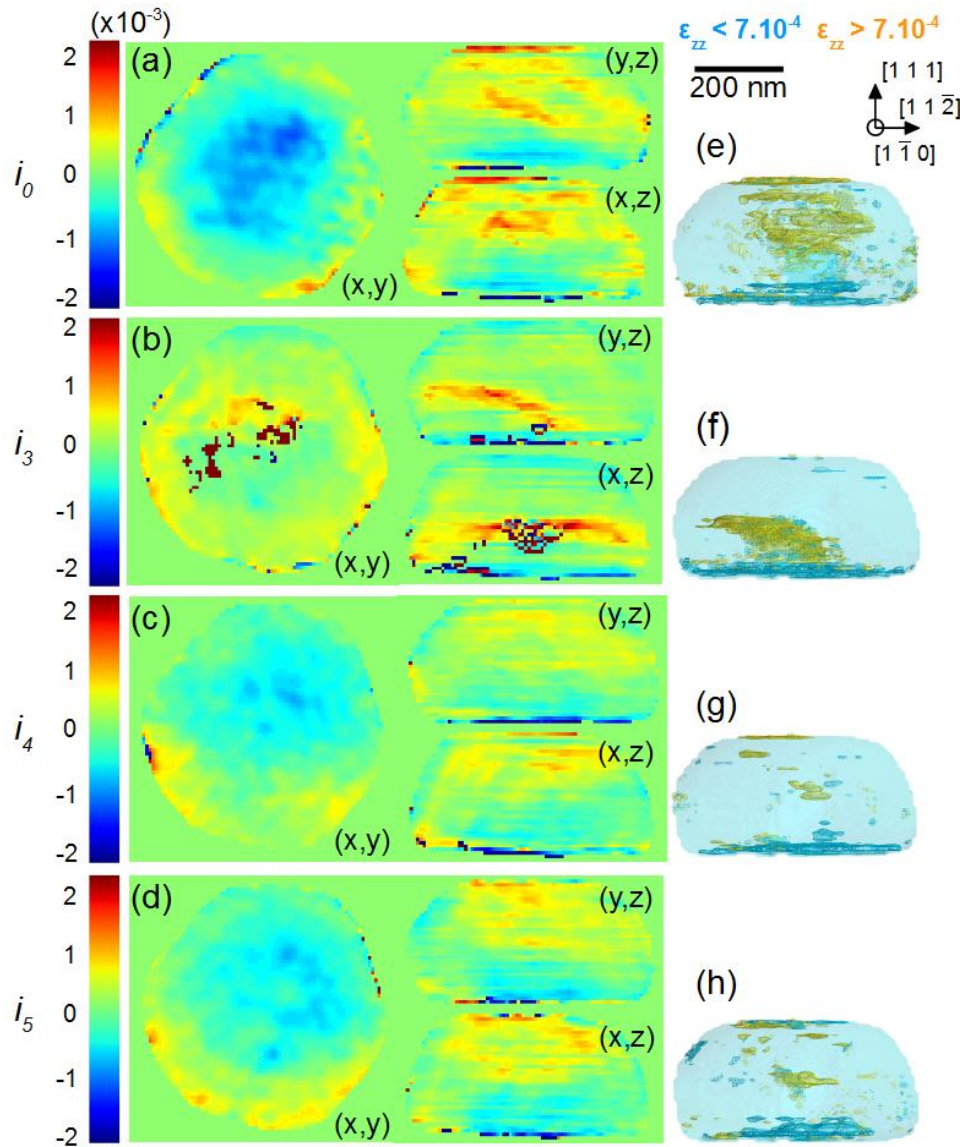


Figure S6 Reconstructed ϵ_{zz} strain field in the (x,y), (x,z) and (y,z) planes corresponding to the (1 1 1), (1 1 -2) and (1 -1 0) planes respectively in the pristine crystal (a) and after 3, 4 and 5 iterative loadings (b-d). Isosurface of the strain drawn for $\epsilon_{zz} < 7.10^{-4}$ (blue) and for $\epsilon_{zz} > 7.10^{-4}$ (orange) in the pristine crystal (e) and after 3,4 and 5 iterative loadings (g-h).

Supporting Information S6: Details of FEM calculations

Here is a more detailed presentation of our FEM calculations:

- A linear anisotropic elasticity law is used. The stiffness tensor of Au is using the following elastic constants in Voigt notation: $C_{11} = 192.34$ GPa, $C_{12} = 163.14$ GPa and $C_{44} = 42.26$ GPa²⁵
- The crystallite geometry is a polyhedral volume defined only by $\{111\}$ and $\{100\}$ facets as in a Wulff equilibrium shape, see fig.5. The extent and location of each facet are obtained from a best fit to the outer shape of the experimental reconstructed data.
- The characteristic size of the FEM mesh is slightly larger than the size of the regular spacing of u_z 3D array obtained from reconstruction. Under those conditions, any finer mesh would not improve the results.
- Quadratic interpolation tetrahedral elements are used in order to best perform gradient calculations from nodal data.
- Surface boundary conditions: two extreme cases are studied. The first one is to consider all surfaces as free surfaces (traction free) but the crystallite-substrate one is considered as rigid (no displacement). The second one considers the crystallite-substrate interface as completely relaxed by some atomic rearrangement so that it behaves also as a free surface.

References

- (1) Amram, D.; Rabkin, E. *Acta Mater.* **2013**, *61*, 4113–4126.
- (2) Chahine, G. A.; Richard, M.-I.; Homs-Regojo, R. A.; Tran-Caliste, T. N.; Carbone, D.; Jacques, V. L. R.; Grifone, R.; Boesecke, P.; Katzer, J.; Costina, I.; *et al.* *J. Appl. Crystallogr.* **2014**, *47*, 762–769.
- (3) Clark, J. N.; Beitra, L.; Xiong, G.; Higginbotham, A.; Fritz, D. M.; Lemke, H. T.; Zhu, D.; Chollet, M.; Williams, G. J.; Messerschmidt, M.; *et al.* *Science* **2013**, *341*, 56–59.
- (4) Harder, R.; Pfeifer, M. A.; Williams, G. J.; Vartianants, I. A.; Robinson, I. K. *Phys. Rev. B* **2007**, *76*.
- (5) Schroer, C. G.; Boye, P.; Feldkamp, J. M.; Patommel, J.; Schropp, A.; Schwab, A.; Stephan, S.; Burghammer, M.; Schöder, S.; Riekkel, C. *Phys. Rev. Lett.* **2008**, *101*.
- (6) Takahashi, Y.; Nishino, Y.; Tsutsumi, R.; Kubo, H.; Furukawa, H.; Mimura, H.; Matsuyama, S.; Zettsu, N.; Matsubara, E.; Ishikawa, T.; *et al.* *Phys. Rev. B* **2009**, *80*, 054103.
- (7) Mastropietro, F.; Carbone, D.; Diaz, A.; Eymery, J.; Sentenac, A.; Metzger, T. H.; Chamard, V.; Favre-Nicolin, V. *Opt. Express* **2011**, *19*, 19223–19232.
- (8) Diaz, A.; Mocuta, C.; Stangl, J.; Mandl, B.; David, C.; Vila-Comamala, J.; Chamard, V.; Metzger, T. H.; Bauer, G. *Phys. Rev. B* **2009**, *79*.
- (9) Rodenburg, J. M.; Hurst, A. C.; Cullis, A. G.; Dobson, B. R.; Pfeiffer, F.; Bunk, O.; David, C.; Jefimovs, K.; Johnson, I. *Phys. Rev. Lett.* **2007**, *98*.
- (10) Favre-Nicolin, V.; Coraux, J.; Richard, M.-I.; Renevier, H. *J. Appl. Crystallogr.* **2011**, *44*, 635–640.
- (11) Fienup, J. R. *Opt. Lett.* **1978**, *3*, 27–29.
- (12) Fienup, J. R. *Appl. Opt.* **1982**, *21*, 2758–2769.
- (13) Marchesini, S.; He, H.; Chapman, H. N.; Hau-Riege, S. P.; Noy, A.; Howells, M. R.; Weierstall, U.; Spence, J. C. H. *Phys. Rev. B* **2003**, *68*.
- (14) Köhl, M.; Minkevich, A. A.; Baumbach, T. *Opt. Express* **2012**, *20*, 17093–17106.
- (15) Labat, S.; Richard, M.-I.; Dupraz, M.; Gailhanou, M.; Beutier, G.; Verdier, M.; Mastropietro, F.; Cornelius, T. W.; Schüllli, T. U.; Eymery, J.; *et al.* *ACS Nano* **2015**, *9*, 9210–9216.
- (16) Chapman, H. N.; Barty, A.; Bogan, M. J.; Boutet, S.; Frank, M.; Hau-Riege, S. P.; Marchesini, S.; Woods, B. W.; Bajt, S.; Benner, W. H.; *et al.* *Nat. Phys.* **2006**, *2*, 839–843.
- (17) Yau, A.; Cha, W.; Kanan, M. W.; Stephenson, G. B.; Ulvestad, A. *Bragg Science* **2017**, *356*, 739–742.
- (18) Ulvestad, A.; Welland, M. J.; Cha, W.; Liu, Y.; Kim, J. W.; Harder, R.; Maxey, E.; Clark, J. N.; Highland, M. J.; You, H.; *et al.* *Nat. Mater.* **2017**, *16*, 565–571.
- (19) Chang, H.-J.; Fivel, M.; Rodney, D.; Verdier, M. *Comptes Rendus Phys.* **2010**, *11*, 285–292.
- (20) Mishin, Y.; Farkas, D.; Mehl, M. J.; Papaconstantopoulos, D. A. *Phys. Rev. B* **1999**, *59*, 3393–3407.
- (21) Williams, D. B.; Carter, C. B. *The Transmission Electron Microscope*. In *Transmission Electron Microscopy*; Springer US, 1996; pp. 3–17.
- (22) Head, A. K. *Aust. J. Phys.* **1967**, *20*, 557–566.
- (23) Steeds, J. W. *Proc. R. Soc. Lond. Math. Phys. Eng. Sci.* **1966**, *292*, 343–373.

- (24) Dupraz, M.; Beutier, G.; Rodney, D.; Mordehai, D.; Verdier, M. *J. Appl. Crystallogr.* **2015**, *48*, 621–644.
- (25) Simmons, G.; Wang, H. *Single Crystal Elastic Constants and Calculated Aggregate Properties.* **1971**.